

# Broad plumes rooted at the base of the Earth's mantle beneath major hotspots

Scott W. French<sup>1</sup>† & Barbara Romanowicz<sup>1,2,3</sup>

**Plumes of hot upwelling rock rooted in the deep mantle have been proposed as a possible origin of hotspot volcanoes, but this idea is the subject of vigorous debate<sup>1,2</sup>. On the basis of geodynamic computations, plumes of purely thermal origin should comprise thin tails, only several hundred kilometres wide<sup>3</sup>, and be difficult to detect using standard seismic tomography techniques. Here we describe the use of a whole-mantle seismic imaging technique—combining accurate wavefield computations with information contained in whole seismic waveforms<sup>4</sup>—that reveals the presence of broad (not thin), quasi-vertical conduits beneath many prominent hotspots. These conduits extend from the core–mantle boundary to about 1,000 kilometres below Earth's surface, where some are deflected horizontally, as though entrained into more vigorous upper-mantle circulation. At the base of the mantle, these conduits are rooted in patches of greatly reduced shear velocity that, in the case of Hawaii, Iceland and Samoa, correspond to the locations of known large ultralow-velocity zones<sup>5–7</sup>. This correspondence clearly establishes a continuous connection between such zones and mantle plumes. We also show that the imaged conduits are robustly broader than classical thermal plume tails, suggesting that they are long-lived<sup>8</sup>, and may have a thermochemical origin<sup>9–11</sup>. Their vertical orientation suggests very sluggish background circulation below depths of 1,000 kilometres. Our results should provide constraints on studies of viscosity layering of Earth's mantle and guide further research into thermochemical convection.**

More than 40 years ago, Morgan<sup>1</sup> proposed that hotspot volcanoes are the surface expression of narrow plumes of hot material that originate in a boundary layer in the deep mantle, as one would expect of a convecting fluid that is heated from below<sup>3</sup>. Whether deep mantle plumes exist, and how deep their roots are, has been the subject of lively debate, which continues to this day. The idea that hotspots may be anchored at the core–mantle boundary (CMB) is supported by several observations: the relative fixity of hotspots with respect to global mantle circulation<sup>1</sup>; the correlation of hotspot locations with the large low shear velocity provinces (LLSVPs) at the base of the mantle<sup>12</sup>; and a suggestion from geodynamic modelling<sup>13</sup> that hotspots might preferentially occur above ultralow velocity zones (ULVZs). A radically different origin for hotspots has also been proposed, in which these features are the consequence of melting owing to shallow convective processes, with their morphologies controlled by stresses and cracks within the lithosphere<sup>2</sup>.

In the classical view<sup>3</sup>, a mantle plume is composed of a large head and a thin tail, which connects it to a root deeper in the mantle. If such plumes were to originate at the base of the mantle, we would expect the lower mantle to contain narrow (less than 200 km in diameter, according to relevant scaling relations<sup>14</sup>), continuous, vertically oriented columns of hotter-than-average (and therefore of low seismic velocity) material, located in the vicinity of presently active hotspots.

In the deep mantle, short-wavelength, low-velocity anomalies are difficult to image with standard seismic tomographic techniques, which typically rely on travel times of body waves (seismic waves that travel

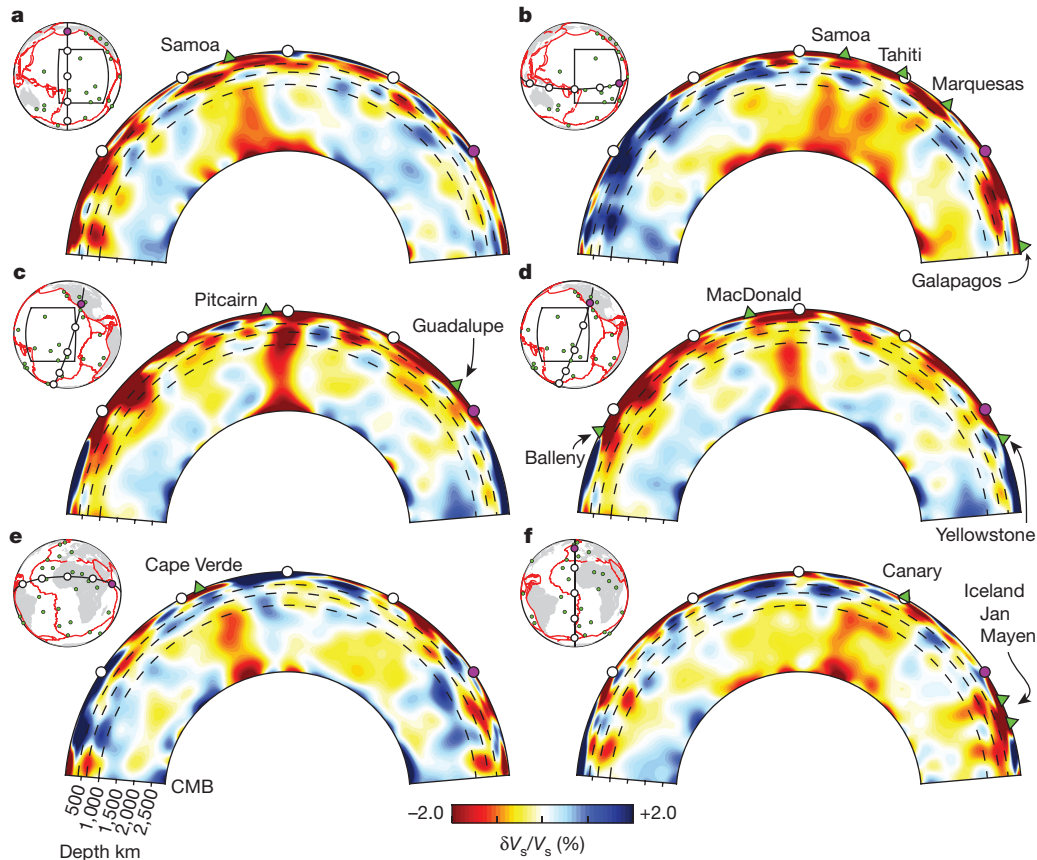
through the interior of Earth); such anomalies can be hidden from view by wavefront healing effects<sup>15</sup>. Also, most hotspot volcanoes, and potentially any associated plumes, are located in the middle of oceans, where they are difficult to image owing to the lack both of dense seismic networks and of earthquakes with the appropriate geometry.

Thus, while various tomographic studies have hinted at the presence of plume-like features in the lower mantle associated with some subset of the major hotspots<sup>16–18</sup>, ambiguity remains as to the vertical continuity of these features, how distinct they are from other low-velocity 'blobs' in the lower mantle, and whether they represent detection of the narrow type of plumes typically associated with purely thermal convection<sup>19</sup>. To improve the resolution of low-velocity features of limited lateral extent such as plumes, two ingredients are needed: first, better illumination of Earth's interior; and second, improved theoretical description of the interaction of the seismic wavefield with the three-dimensional Earth structure.

Here we present robust evidence for large, vertically continuous, low-velocity columns in the lower mantle beneath many prominent hotspots, from our recent global, radially anisotropic, whole-mantle shear-wave velocity model, SEMUCB-WM1 (ref. 4). This model was constructed by inversion of a large data set of full, long-period seismograms, including first- and second-orbit fundamental mode and overtone surface waves down to 60 s, as well as body waveforms down to 32 s. Because it includes surface-wave overtones, shear waves diffracted along the core–mantle boundary ( $S_{\text{diff}}$ ) and multiply-reflected waves between the surface and the CMB, this data set provides considerably better illumination of the whole-mantle volume than can be obtained with a standard set of travel times alone. In addition, accurate numerical computation of the forward wavefield using the spectral element method<sup>20</sup> at each iteration of the model construction allows us to better resolve regions of lower-than-average shear-wave velocity, as previously illustrated for the upper mantle<sup>21</sup>. The construction of this model is briefly summarized in the Methods.

In model SEMUCB-WM1 (ref. 4), broad, dome-like plumes that show a reduction of shear-wave velocity by more than 1.5%–2% are present in the lower mantle beneath Samoa, Hawaii and the Pacific Superswell volcanoes. These plumes are clearly distinct from other, more isolated and weaker low-velocity features that appear in cross-sections spanning half of Earth's circumference (Fig. 1). The plumes are rooted in patches of more strongly reduced shear-wave velocity near the CMB, and extend vertically up to depths of at least 1,000 km, above which their character changes. A three-dimensional view of the central Pacific region (Fig. 2) shows that the cores of these plumes are well separated from each other across most of the lower mantle, embedded in the lower-than-average-velocity background of the Pacific LLSVP. This is particularly clear in the depth range 1,000 km to 1,500 km, where there is a one-to-one relationship with the corresponding hotspot volcanoes, although the plumes are not always located exactly beneath the volcanoes. Comparison with previous global models (Extended Data Fig. 1) indicates general agreement on the background long-wavelength features, while in SEMUCB-WM1 the

<sup>1</sup>Department of Earth and Planetary Science, Berkeley Seismological Laboratory, University of California at Berkeley, California 94720, USA. <sup>2</sup>Institut de Physique du Globe, Paris 75238, France. <sup>3</sup>Collège de France, Paris 75005, France. †Present address: National Energy Research Scientific Computing Center, Lawrence Berkeley National Laboratory, Berkeley, California 94720, USA.



**Figure 1 | Whole-mantle depth cross-sections of relative shear-velocity variations in model SEMUCB-WM1, in the vicinity of major hotspots.** The sections are shown in the inset maps, with the direction of the projection indicated by the position of the purple dot in both map and cross-section views (black boxes correspond to the three-dimensional rendering regions in Fig. 2). Green dots and triangles mark the locations of hotspots<sup>27</sup>. The reference model is the corresponding global one-dimensional average shear-wave velocity ( $V_s$ ) profile of SEMUCB-WM1. The colour scale has been chosen to emphasize lower-mantle structures, resulting in substantial saturation in the upper mantle. Broken lines indicate depths of 410 km, 660 km and 1,000 km. Focused, quasi-vertical, broad plumes extend continuously from

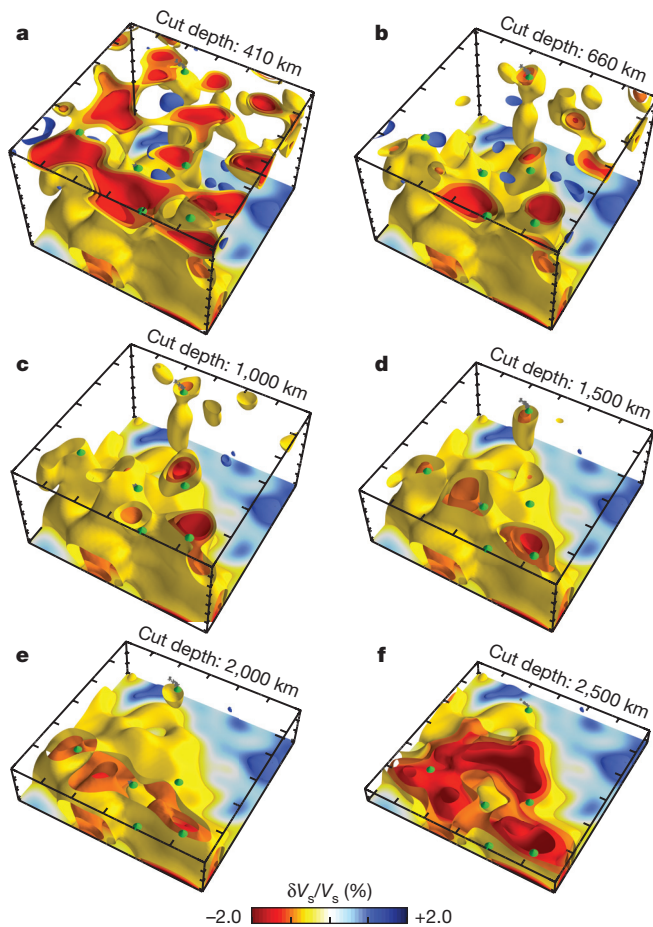
plumes stand out as continuous features confined to well defined vertically oriented columns.

In particular, the Hawaiian plume appears as a separate vertical conduit of varying width (Fig. 2a–c), with a weaker zone at around 500 km above the CMB, rooted in its own patch of strongly reduced shear velocity at the base of the mantle. In the transition zone, this plume appears to be strongly deflected towards the west–southwest (Fig. 3). This morphology is compatible with evidence for a hot upper mantle to the west of Hawaii, based on the analysis of converted waves (that is, receiver functions)<sup>22</sup>. The presence of bodies with higher-than-average velocity southwest and northeast of the Hawaiian chain is in agreement with regional studies<sup>23,24</sup>. However, in the lower mantle, the associated conduit is more vertically oriented in SEMUCB-WM1. Similar broad, vertically oriented low-velocity conduits are found in the vicinity of some hotspots lying on the border of the African LLSVP (Figs 1e, f and 3d, e and Extended Data Fig. 2).

The lower-mantle plume conduits described above are rooted in wide patches (of diameter 500–800 km) of strongly negative velocity reduction near the CMB. In at least three cases, these patches coincide in location with large ULVZs previously detected in the vicinity of the corresponding hotspots: near Hawaii (detected through observations of post-cursors to diffracted S waves<sup>5</sup>), and beneath Iceland<sup>6</sup> and Samoa<sup>7</sup> (found through the study of waveform distortion in the phase SP<sub>diff</sub>KS).

patches of strongly reduced  $V_s$  at the base of the mantle to depths of at least 1,000 km in the vicinity of: **a**, Samoa; **b**, Tahiti, the Marquesas, the Galapagos and Samoa; **c**, Pitcairn; **d**, MacDonal; **e**, Cape Verde; and **f**, the Canary Islands. These plumes stand out from other low-velocity features in these cross-sections, which span nearly half of Earth. **d**, Note the absence of a noticeable anomaly in the lower mantle immediately beneath the Yellowstone hotspot. However, a faint low-velocity conduit appears to the southwest (offshore of North America), anchored by a low-velocity patch in the D' mantle region. It is beyond the resolution of our study to verify whether this feature is related to the Yellowstone or the Guadalupe (c) hotspot.

Because of the computational challenges of whole-mantle imaging using full waveforms and numerical simulations, the resolution of our model is limited by our choice of parametrization and maximum frequency. However, resolution tests (Methods; Extended Data Figs 4–8) clearly indicate that our approach can resolve the vertical continuity of plumes without ray-like smearing or erroneous deflection, and that the variations of the shape and amplitude of the plumes with depth are likely to be robust features. These tests also indicate (see Supplementary Information section S1 and Supplementary Figs 1 and 2) that our modelling approach can distinguish between hypothetical broad superplume-like features and the distinct vertical conduits that are shown in Fig. 1. Numerical experiments (Supplementary Information section S2 and Supplementary Figs 5–9) demonstrate that plumes of the same scale as are seen in Fig. 1 and used in our tests should be readily detectable in the waveform data used by our inversion. Furthermore, on the basis of relative amplitude recovery alone, our resolution tests also show that in order to obtain a velocity reduction of 2% or more over the major part of the lower mantle—as seen in our model—a narrow plume would have to be very strong (that is, >10% reduction in shear-wave velocity for a plume of width <200 km; see Methods and Extended Data Fig. 4). Such a strong velocity contrast would translate into unrealistically high<sup>25</sup> effective temperature excesses of 1,500–2,000 °C. In contrast, for a 2% velocity anomaly over a width of 800–1,000 km, as imaged in SEMUCB-WM1 under Hawaii



**Figure 2 | Three-dimensional rendering of shear-wave-velocity structure in the Pacific Superswell region.** Relative velocity perturbations are shown with respect to the global average at each depth. For each panel, the location of the box is shown in the inset map of Fig. 1. The region is shown from above, with cuts at increasing depths: **a**, 410 km; **b**, 660 km; **c**, 1,000 km; **d**, 1,500 km; **e**, 2,000 km; **f**, 2,500 km. The following hotspot locations, projected down from the surface, are indicated by green cones in each box: Hawaii (top; north), Samoa (left; west), and the four Superswell hotspots: Tahiti, Pitcairn, Marquesas and MacDonal. Well defined vertically oriented conduits with central cores of velocity lower than  $-1.5\%$  can be associated with each of the hotspots, particularly clearly in **c** and **d**. The low-velocity conduit beneath Hawaii stands out in **b–d**. In **f**, patches of much lower-than-average velocity start appearing within the Pacific LLSVP, continuing down to the CMB. On the other hand, at a depth of 410 km, the low-velocity conduits start spreading horizontally and merge into the depth range in which low-velocity fingers have previously been observed in the upper mantle<sup>21</sup>.

(Fig. 3), effective temperature excesses of 400–500 °C (estimated in a similar manner) are plausible, if one considers that the plumes are rooted in a chemically dense layer<sup>9</sup>. Whether or not these plumes entrain much chemical heterogeneity to the upper mantle is beyond the resolution of this study; however, their width and vertically varying shapes are compatible with models of thermochemical plumes<sup>10,11</sup>.

Clearly resolved plumes with similar characteristics are found beneath 11 major hotspots (Fig. 4 and Extended Data Table 1). Visual inspection of the SEMUCB-WM1 model suggests the presence of weaker conduits extending from the CMB through most of the lower mantle beneath several other hotspots. Taken together, this ensemble of hotspots includes all of those classified as ‘primary’ in ref. 26. Interestingly, all of the plumes we detected are located within or at the borders of the African and Pacific LLSVPs. In contrast, we found no deep-mantle expression of those hotspots<sup>26,27</sup> that are located above faster-than-average shear-wave velocities in the mantle region next to the CMB (the D’ region). This may indicate either that the

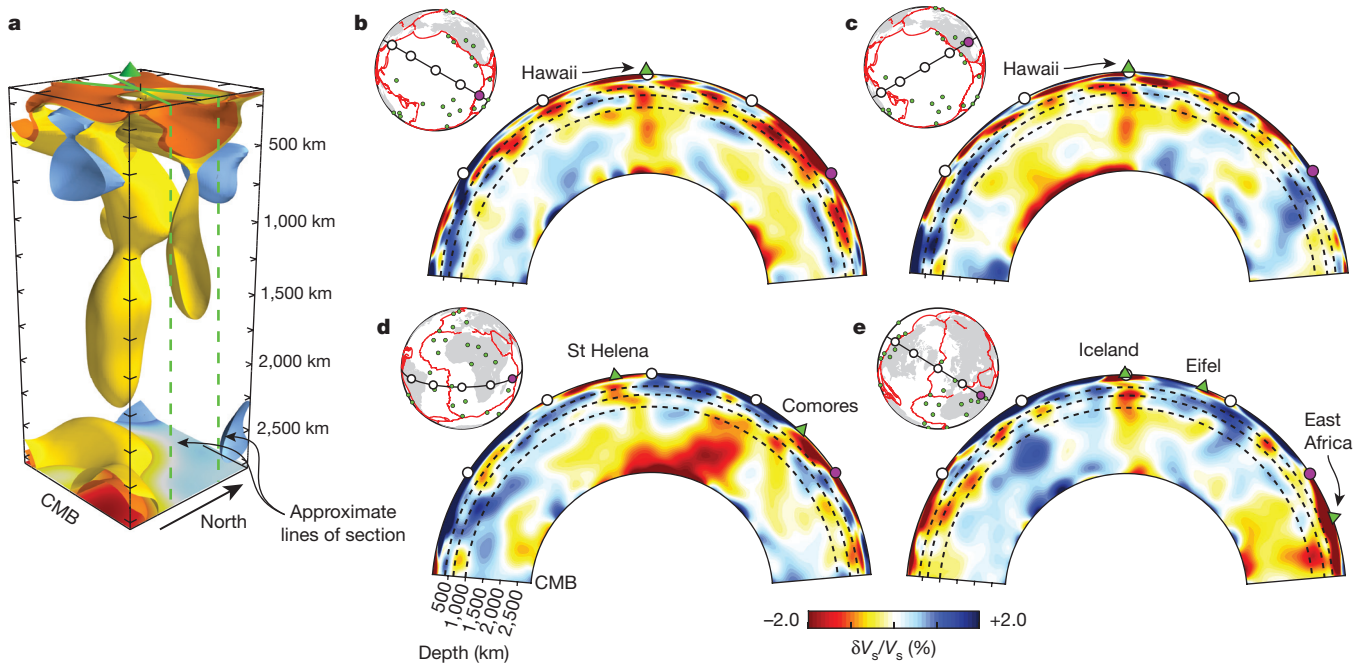
corresponding plumes are below the detection capabilities of our current modelling approach in the lower mantle, or that they originate in the upper mantle or the uppermost lower mantle. This is the case, in particular, for the Yellowstone hotspot (Fig. 1d). In the case of the Bowie/Juan de Fuca hotspots, the low-velocity anomaly can be followed to the base of the upper mantle<sup>28</sup>, but not below. Likewise, most of the North African hotspots (except Afar and the neighbouring East African Rift system, particularly beneath Tanzania) have no clear lower-mantle expression. Instead, they appear to derive from a very broad lower-mantle dome, much further south, associated with the African LLSVP (Fig. 3d and Extended Data Fig. 3). The difference in morphology of the Pacific (bundle of plumes) and African (broad dome) LLSVPs, which has been suggested previously<sup>29</sup>, is now very clear.

Our results confirm the presence of broad plume-like conduits in the lower mantle, located in the vicinity of major hotspots<sup>4,17</sup>. For the first time, to our knowledge, our study establishes their quasi-vertical continuity from about 1,000-km depth down to the CMB, where they are rooted in patches or domes of much lower-than-average shear velocity, at least some of which (in Iceland, Hawaii and Samoa) coincide with the location of known ULVZs. These plumes exhibit other common characteristics. They are remarkably vertical, indicating that they are not strongly affected by a lower-mantle wind<sup>27</sup>, and may represent the primary upwellings in the lower mantle. They often have a pinched zone between 500 km and 1,000 km above the CMB—a shape that is similar to what may be expected for thermochemical plumes<sup>10,11</sup>.

Interestingly, the character of the anomaly appears to change at a depth of around 1,000 km: some plumes are shifted horizontally (for example, Pitcairn and St Helena); others become thinner (such as Samoa and Tahiti); and yet others cannot clearly be tracked to shallower depths (for example, Cape Verde), indicating that they may have split into narrower conduits<sup>4,18</sup> that, in some cases, are below the resolution of our model. In Iceland and Hawaii (Fig. 3), horizontally elongated arms branch out from the plume stem just below 1,000 km, suggesting that the flow may have encountered resistance to direct continuation into the upper mantle. Similarly, we observe what appears to be ponding of low-velocity material beneath 1,000 km (for example at the Canary Islands; Fig. 1f). This is also the depth range in which some slabs appear to stagnate<sup>30</sup>. Those plumes that we can track to shallower depths appear to meander through the upper mantle and, in many cases, connect to the previously observed low-velocity channels in the depth range 200–400 km (ref. 21; see, for example, Pitcairn in Figs 1 and 2).

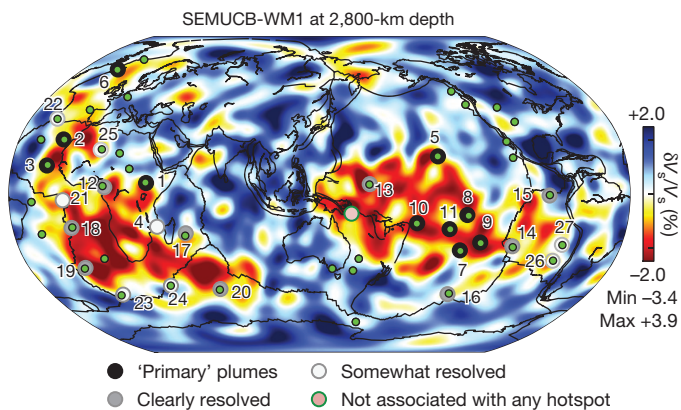
The observed characteristics of these seismically imaged plumes should provide improved constraints on our understanding of the viscosity structure and dynamics of the mantle. The direct connection of these plumes with ULVZs on the one hand, and with prominent hotspots on the other, suggests that the plumes are long-lived and contain material originating in the D’ region that is of lower viscosity than the bulk lower mantle<sup>8</sup>. The change of character at a depth of 1,000 km—taken together with the stagnation of some subducted slabs<sup>30</sup>—suggests the presence of a notable change in viscosity around that depth. The variation in amplitude and width of these velocity anomalies in the lower mantle may be related to the stage of development of the plumes<sup>10,11</sup>, or to variations of the viscosity structure with depth<sup>31,32</sup>, or to a combination of viscosity structure and density contrast owing to chemical heterogeneity at the base of the mantle<sup>11</sup>. The dominantly vertical character of the plumes in the lower mantle indicates that circulation may be very sluggish away from the plumes. The often-invoked mantle wind<sup>27</sup> would be largely confined to the upper mantle, where plumes may indeed become entrained with a substantial non-vertical component (for example, at Pitcairn and Hawaii) into the more vigorous secondary-scale convection that is probably driven by plate motions<sup>21</sup>.

Our study demonstrates the potential of combining waveform tomography with accurate modelling of wave propagation in



**Figure 3 | Hawaii, Iceland, St Helena and the African superplume.** **a**, Three-dimensional rendering of the Hawaiian plume, viewed from the southeast. In the lower mantle, the plume conduit is vertically oriented, rooted in a patch of very low  $V_s$  at the base of the mantle, with a weak zone in the depth range 2,300–2,600 km. Above approximately 1,000 km, the conduit is deflected towards the west into the transition zone, and appears to interact with the low-velocity finger oriented in the Pacific plate absolute plate motion direction<sup>21</sup> visible in cross-section above a depth of 500 km. **b–e**, Two-dimensional vertical cross-sections along planes as indicated in the inset maps and corresponding broken green lines in **a**, represented in the same way as in Fig. 1. In **c**, in the

lowermost mantle between the two westernmost reference white dots, we see the edge of the plume associated with the Caroline hotspot. Subduction zones are well imaged in the western Pacific (**b, c**), spreading above the 1,000-km horizon, and in south America (**d**); in **c** and **e**, the fossil Farallon subduction extends through the lower mantle. Blue zones in the vicinity of Hawaii in the lower mantle may potentially be downwellings corresponding to other fossil slabs, although this warrants further study. In **e**, we note the particularly broad African plume, one lobe of which extends to the mantle transition zone, the other giving rise in the mid lower mantle to a thinner, weaker plume beneath St Helena.



**Figure 4 | Locations of plumes detected in the lower mantle in model SEMUCB-WM1<sup>4</sup>.** The background map represents the relative  $V_s$  variations at 2,800 km in this model, with respect to the global average at that depth. We identify three categories of plumes. ‘Primary’ plumes are those for which  $\delta V_s/V_s$  is lower than  $-1.5\%$  for most of the depth interval 1,000–2,800 km. These 11 plumes also correspond to regions of the lower mantle where the average velocity reduction over the depth range 1,000–1,800 km is significant at the  $2\sigma$  level (see, for example, Supplementary Figs 3 and 4). Clearly resolved plumes correspond to vertically continuous conduits with  $\delta V_s/V_s$  greater than  $-0.5\%$  in the depth range 1,000–2,800 km. Somewhat resolved plumes have vertically trending conduits with  $\delta V_s/V_s$  greater than  $-0.5\%$  for most of the depth range 1,000–2,800 km, albeit not as clearly continuous. Plumes are numbered as listed in Extended Data Table 1. Green dots represent the global hotspot distribution according to ref. 27. Note that none of the plumes detected falls within a region of faster-than-average velocity at the base of the mantle, and that long-wavelength structure in this model agrees with that of previous tomographic models (see, for example, Supplementary Fig. 10).

order to advance our understanding of the upwelling part of deep mantle flow and its relationship to surface observations. While thin ‘classical’ plume tails may exist in the mantle, they remain below the resolution of global tomography at present. However, our robust confirmation of the existence of broad, possibly thermochemical, plumes—associated with prominent hotspots and rooted in the D’ region (at least some of them in ULVZs)—should provide important constraints for further geodynamical modelling of present-day mantle circulation, and for Earth’s heat-flux budget<sup>33</sup>.

**Online Content** Methods, along with any additional Extended Data display items and Source Data, are available in the online version of the paper; references unique to these sections appear only in the online paper.

Received 12 November 2014; accepted 19 June 2015.

- Morgan, W. J. Convection plumes in the lower mantle. *Nature* **230**, 42–43 (1971).
- Anderson, D. L. Scoring hotspots: the plume and plate paradigms. *Geol. Soc. Special Papers* **388**, 31–54 (2005).
- Campbell, I. H. & Griffiths, R. W. Implications of mantle plume structure for the evolution of flood basalts. *Earth Planet. Sci. Lett.* **99**, 79–93 (1990).
- French, S. W. & Romanowicz, B. A. Whole-mantle radially anisotropic shear velocity structure from spectral-element waveform tomography. *Geophys. J. Int.* **199**, 1303–1327 (2014).
- Cottaar, S. & Romanowicz, B. An unusually large ULVZ at the base of the mantle near Hawaii. *Earth Planet. Sci. Lett.* **355–356**, 213–222 (2012).
- Helmlinger, D. V., Wen, L. & Ding, X. Seismic evidence that the source of the Iceland hotspot lies at the core-mantle boundary. *Nature* **396**, 251–255 (1998).
- Thorne, M. S., Garnero, E. J., Jahnke, G., Igel, H. & McNamara, A. Mega ultra low velocity zone and mantle flow. *Earth Planet. Sci. Lett.* **364**, 59–67 (2013).
- Jellinek, A. M. & Manga, M. The influence of a chemical boundary layer on the fixity, spacing and lifetime of mantle plumes. *Nature* **418**, 760–763 (2002).
- Farnetani, C. G. Excess temperature of mantle plumes: the role of chemical stratification across D’. *Geophys. Res. Lett.* **24**, 1583–1586 (1997).

10. Lin, S.-C. & van Keken, P. E. Dynamics of thermochemical plumes: 2. Complexity of plume structures and its implications for mapping mantle plumes. *Geochem. Geophys. Geosyst.* **7**, Q03003 (2006).
11. Kumagai, I., Davaille, A., Kurita, K. & Stutzmann, E. Mantle plumes: thin, fat, successful or failing? Constraints to explain hot spot volcanism through time and space. *Geophys. Res. Lett.* **35**, L16301 (2008).
12. Thorne, M. S., Garnero, E. J. & Grand, S. P. Geographic correlation between hot spots and deep mantle lateral shear-wave velocity gradients. *Phys. Earth Planet. Inter.* **146**, 47–63 (2004).
13. McNamara, A. K., Garnero, E. J. & Rost, S. Tracking deep mantle reservoirs with ultra-low velocity zones. *Earth Planet. Sci. Lett.* **299**, 1–9 (2010).
14. Davaille, A. & Limare, A. in *Treatise on Geophysics* Vol. 7 (ed. Bercovici, D.) 89–156 (Elsevier, 2007).
15. Nolet, G. & Dahlen, F. A. Wavefront healing and the evolution of seismic delay times. *J. Geophys. Res.* **105**, 19043–19054 (2000).
16. Zhao, D. Global tomographic images of mantle plumes and subducting slabs: insight into deep earth dynamics. *Phys. Earth Planet. Inter.* **146**, 3–34 (2004).
17. Montelli, R. *et al.* Finite-frequency tomography reveals a variety of plumes in the mantle. *Science* **303**, 338–343 (2004).
18. Suetsugu, D. *et al.* South Pacific mantle plumes imaged by seismic observation on islands and seafloor. *Geochem. Geophys. Geosyst.* **10**, Q11014 (2009).
19. Boschi, L., Becker, T. W. & Steinberger, B. On the statistical significance of correlations between synthetic mantle plumes and tomographic models. *Phys. Earth Planet. Inter.* **167**, 230–238 (2008).
20. Capdeville, Y., Chaljub, E., Vilotte, J. P. & Montagner, J. P. Coupling the spectral element method with a modal solution for elastic wave propagation in global earth models. *Geophys. J. Int.* **152**, 34–67 (2003).
21. French, S. W., Lekic, V. & Romanowicz, B. Waveform tomography reveals channeled flow at the base of the oceanic asthenosphere. *Science* **342**, 227–230 (2013).
22. Li, X. *et al.* Mapping the Hawaiian plume conduit with converted seismic waves. *Nature* **405**, 939–941 (2000).
23. Wolfe, C. J. *et al.* Mantle P-wave velocity structure beneath the Hawaiian hotspot. *Earth Planet. Sci. Lett.* **303**, 267–280 (2011).
24. Laske, G. *et al.* Asymmetric shallow mantle structure beneath the Hawaiian Swell—evidence from Rayleigh waves recorded by the PLUME network. *Geophys. J. Int.* **187**, 1725–1742 (2011).
25. Albers, M. & Christensen, U. The excess temperature of plumes rising from the core mantle boundary. *Geophys. Res. Lett.* **23**, 3567–3570 (1996).
26. Courtillot, V., Davaille, A., Besse, J. & Stutzmann, E. Three distinct types of hotspots in the Earth's mantle. *Earth Planet. Sci. Lett.* **205**, 295–308 (2003).
27. Steinberger, B. Plumes in a convecting mantle: models and observations for individual hotspots. *J. Geophys. Res.* **105**, 11127–11152 (2000).
28. Nataf, H. C. & VanDecar, J. Seismological detection of a mantle plume? *Nature* **364**, 115–120 (1993).
29. Su, W. J., Woodward, R. L. & Dziewonski, A. M. Degree 12 model of shear velocity heterogeneity in the mantle. *J. Geophys. Res.* **99**, 6945–6980 (1994).
30. Fukao, Y. & Obayashi, M. Subducted slabs stagnant above, penetrating through, and trapped below the 660 km discontinuity. *J. Geophys. Res.* **118**, 1–19 (2013).
31. Forte, A. M. & Mitrovica, J. K. Deep mantle high viscosity flow and thermochemical structure inferred from seismic and geodetic data. *Nature* **410**, 1049–1056 (2001).
32. Marquardt, H. & Miyagi, L. Slab stagnation in the shallow lower mantle due to an increase in mantle viscosity. *Nature Geosci.* **8**, 311–314 (2015).
33. Nolet, G., Karato, S. I. & Montelli, R. Plume fluxes from seismic tomography. *Earth Planet. Sci. Lett.* **248**, 685–699 (2006).

**Supplementary Information** is available in the online version of the paper.

**Acknowledgements** We thank the IRIS Data Management Center for providing the waveform data used in this study. This study was supported by an NSF Graduate Research Fellowship to S.W.F., NSF grant EAR-1417229, and ERC Advanced Grant WAVETOMO. Computations were performed at the National Energy Research Scientific Computing Center, supported by the US Department of Energy Office of Science (contract DE-AC02-05CH11231).

**Author Contributions** B.R. and S.W.F. collaborated in developing the concept of this paper. B.R. wrote the first draft, which was jointly finalized through successive iterations. S.W.F. is responsible for most of the technical aspects of this work, including the realization of most of the figures, with input from B.R. on figure design. B.R. is responsible for Fig. 4 and Extended Data Table 1.

**Author Information** Reprints and permissions information is available at [www.nature.com/reprints](http://www.nature.com/reprints). The authors declare no competing financial interests. Readers are welcome to comment on the online version of the paper. Correspondence and requests for materials should be addressed to B.R. ([barbara@seismo.berkeley.edu](mailto:barbara@seismo.berkeley.edu)).

## METHODS

**Waveform inversion technique.** As was the case for models SEMum<sup>34</sup> and SEMum2 (ref. 21), model SEMUCB-WM1<sup>4</sup> was developed using a time-domain waveform inversion technique that combines highly accurate spectral-element forward wavefield modelling<sup>35</sup> with efficient sensitivity kernel computation using nonlinear asymptotic coupling theory (NACT)<sup>36</sup>. This approach allows us to take advantage of both the accuracy of computing the misfit function with spectral-element modelling, and the efficiency of NACT-based kernels, which furthermore allow us to use a quickly converging Gauss–Newton scheme. Because the approximate Hessian matrix cannot easily fit in computer memory when considering whole-mantle scale inversions such as SEMUCB-WM1, we designed a high-performance distributed-memory abstraction<sup>37</sup> for its assembly from parallel NACT computations. As with other tomographic approaches, care must be taken in selecting the starting model owing to the strong nonlinearity of the inverse problem. In ref. 34, we explain how the present line of successive tomographic models (SEMum, SEMum2, and now SEMUCB-WM1) started from a one-dimensional earth model, and progressively incorporated more and more waveform data and shorter periods as iterations proceeded and three-dimensional structure became stronger.

**Parameterization and starting model.** Model SEMUCB-WM1 is constructed starting from model SEMum2<sup>21</sup> above about 800-km depth and model SAW24B16<sup>38</sup> from below this depth (also used in the SEMum and SEMum2 inversions to account for lower-mantle structure). We invert for three-dimensional variations in Voigt-average isotropic shear-wave velocity ( $V_s$ ) and the radially anisotropic parameter  $\xi = (V_{sh}/V_{sv})^2$ , with respect to a one-dimensional mean reference model that evolves throughout the inversion. In contrast, the one-dimensional attenuation model is fixed to a smoothed version of QL6 (ref. 39). We express perturbations to mantle  $V_s$  and  $\xi$  in 20 cubic b-splines<sup>38</sup> with variable spacing radially and in spherical splines<sup>40</sup> laterally, with lateral spacing of nodes of less than  $2^\circ$  for  $V_s$  and  $8^\circ$  for  $\xi$ . Source parameters for each event are kept fixed to those reported in the Global CMT catalogue (<http://www.globalcmt.org>). Tests indicate<sup>14</sup> that allowing source perturbations should not measurably affect the resulting structure at the current resolution. From our SEMum2 + SAW24B16 starting model, three inversion iterations were performed, while incrementally incorporating more and shorter-period data (see ‘Data selection and inversion’). We note that the upper-mantle part of the model (down to 400 km) has not significantly changed in this process, further validating the results described in ref. 4.

**Data selection and inversion.** Our approach is described in detail in ref. 4 and includes discussions of how we calibrate our crustal model, introduce prior information in the data and model space, and assess model performance and uncertainties (including resolution and statistical resampling tests). Here we briefly recall details of the iterative inversion process, including the addition of new waveform data and tests of convergence.

While SEMum and SEMum2 included only fundamental and overtone mode surface waveforms at long periods ( $T > 60$  s), here we include body-waveform data. To this end, we assembled a data set comprising full three-component teleseismic waveforms, filtered in multiple passbands, allowing us to incrementally incorporate higher-frequency body-waveform data: 1, surface-wave passband: cut-off at 400 s and 60 s (corners at 250 s and 80 s); 2, body-wave passband (filter I): cut-off at 300 s and 36 s (corners at 180 s and 45 s); and 3, body-wave passband (filter II): cut-off at 300 s and 32 s (corners at 180 s and 38 s). In addition to incorporating shorter periods, we also expanded our data set by incorporating additional events: starting from the 203 events used in developing upper-mantle models SEMum and SEMum2, we added 70 new events with moment magnitude  $M_w = 5.8$ –7.3, chosen to be spatially distributed in a complementary manner to the original set.

The inversion comprised three phases. In phase I, we performed one iteration of inversion for whole-mantle structure using the 60-s surface-waveform and 36-s body waveform data sets (filter I) picked from the 203 events used in developing SEMum and SEMum2, and constraints from surface-wave group-velocity maps between 25 s and 150 s to enforce consistency with our crustal modelling scheme<sup>4</sup>. Because upper-mantle structure changed very little in this first iteration, aside from slightly larger amplitudes following the introduction of the body-waveform data, we chose to invert for structure only at depths greater than 300 km in the remaining iterations (after first recalibrating the crustal model one last time; see ref. 4 for details). In phase II, we introduced the 70 new events. This step involved picking the new-event data, as well as reprocessing the older-event data, using the spectral-element synthetics from the previous iteration (our waveform-data-picking approach selects data on the basis of their similarity to the spectral-element synthetics computed in the most recent iteration model). We then performed another inversion iteration, again using the 60-s and 36-s filter passbands, but now including the new-event data and inverting for structure below 300-km depth only. In phase III, we again reprocessed the data from the complete 273-event data

set, but now using a new shorter-period body-wave passband (filter II). We then inverted for structure below 300 km using the 60-s and 32-s data passbands.

To ensure that our inversion was converging, we determined, after each iteration, whether more waveform windows were selected in the subsequent data-reprocessing round than would have been selected using spectral-element synthetics from the previous-iteration model. By the final iteration, we found only small gains in the numbers of selected windows, indicating that the inversion had probably converged for the particular passbands considered. We also assessed convergence by testing fits to held-out waveforms from ten events not included in the inversion, and found that these validation data exhibited fits quite similar to that seen for the inversion data<sup>4</sup>.

**Computational cost.** For the four rounds of spectral-element simulations required to complete these three phases of inversion (including a last round to assess the final fit to the data), the present study required about three million CPU (central processing unit) hours, performed on Hopper, a Cray XE6 supercomputer at the National Energy Research Scientific Computing Center (NERSC). The NACT-based Hessian estimation and Gauss–Newton model update computations were performed on NERSC Edison, a Cray XC30.

**Resolution and model uncertainties.** It is well known that standard linear resolution analyses are strictly valid only for linear problems (or potentially near the optimum of a nonlinear problem<sup>41</sup>) and may also yield misleading results<sup>42</sup>. However, these remain useful techniques for assessing certain aspects of a tomographic inversions, providing insight into potential issues related to data coverage (for example, uneven sensitivity or smearing), the role of *a priori* information in constraining model smoothness, and limitations of the chosen model basis. We provide an extensive discussion of these aspects of SEMUCB-WM1 in the context of resolution analysis in ref. 4; here we focus on analyses specifically relevant to the types of conduit-like structures discussed in the main text.

**Recovery of whole- and partial-mantle plumes.** One obvious question that can be probed using resolution analysis is whether we can reasonably expect to resolve the plume-like conduits of the amplitude and scale observed in SEMUCB-WM1. In Extended Data Figs 4 and 5, we examine the recovery of synthetic whole- and partial-mantle plumes of diameter 1,000 km and 600 km, beneath Hawaii and Iceland. These synthetic test models have a peak amplitude of  $-2\%$ , comparable to many of the conduits observed in our model, and a cosine-cap lateral amplitude profile (which means that the ‘core’ of each plume, exhibiting anomaly strength  $>1\%$ , is only half of its diameter—500 km and 300 km, respectively). We also examine recovery of plumes truncated at successively greater depths (1,000, 1,500 and 2,000 km) to assess vertical smearing. Artefacts above the truncation depth in the synthetic  $i$  models are due to aliasing phenomena associated with the radial b-spline basis used to parameterize our model (see above). Overall, we find that all whole- and partial-mantle input plumes are recovered quite well beneath both Hawaii, with denser data coverage, and Iceland, with comparatively sparser coverage (there is a slight difference in amplitude recovery beneath the two). We see no evidence of lateral smearing, or (in the case of the truncated plumes) radial smearing, nor do we detect notable gaps in recovery. Recovered amplitudes vary as a function of depth, with comparatively weaker, but still satisfactory, recovery in the less well sampled mid-mantle (about half of the input anomaly strength). Furthermore, as noted in the main text, the pattern of amplitude variation with depth seen in Extended Data Figs 4 and 5 does not match that of our imaged plumes, which often show local amplitude maxima in the mid-mantle (not minima, as suggested by these tests). Thus, while we cannot rule out that spatial variation in sensitivity contributes in some way to the imaged amplitude distribution, these results give us confidence that plumes of similar dimension and amplitude to those seen in SEMUCB-WM1 should be recoverable.

In Extended Data Fig. 6, we consider a narrower plume (400 km in diameter) spanning from the CMB to 1,000-km depth, with a peak amplitude of  $-2\%$ . We observe that the output structure is at least 800 km in width, but is also significantly weaker than the input, exhibiting a maximum amplitude of  $-0.6\%$  near its base, while only reaching  $-0.3\%$  or  $-0.4\%$  elsewhere in its core, indicating that an actual plume of width less than 400 km would have to be much stronger to be properly detected in our model (see further discussion in ‘Estimated excess temperatures and actual width of plumes’).

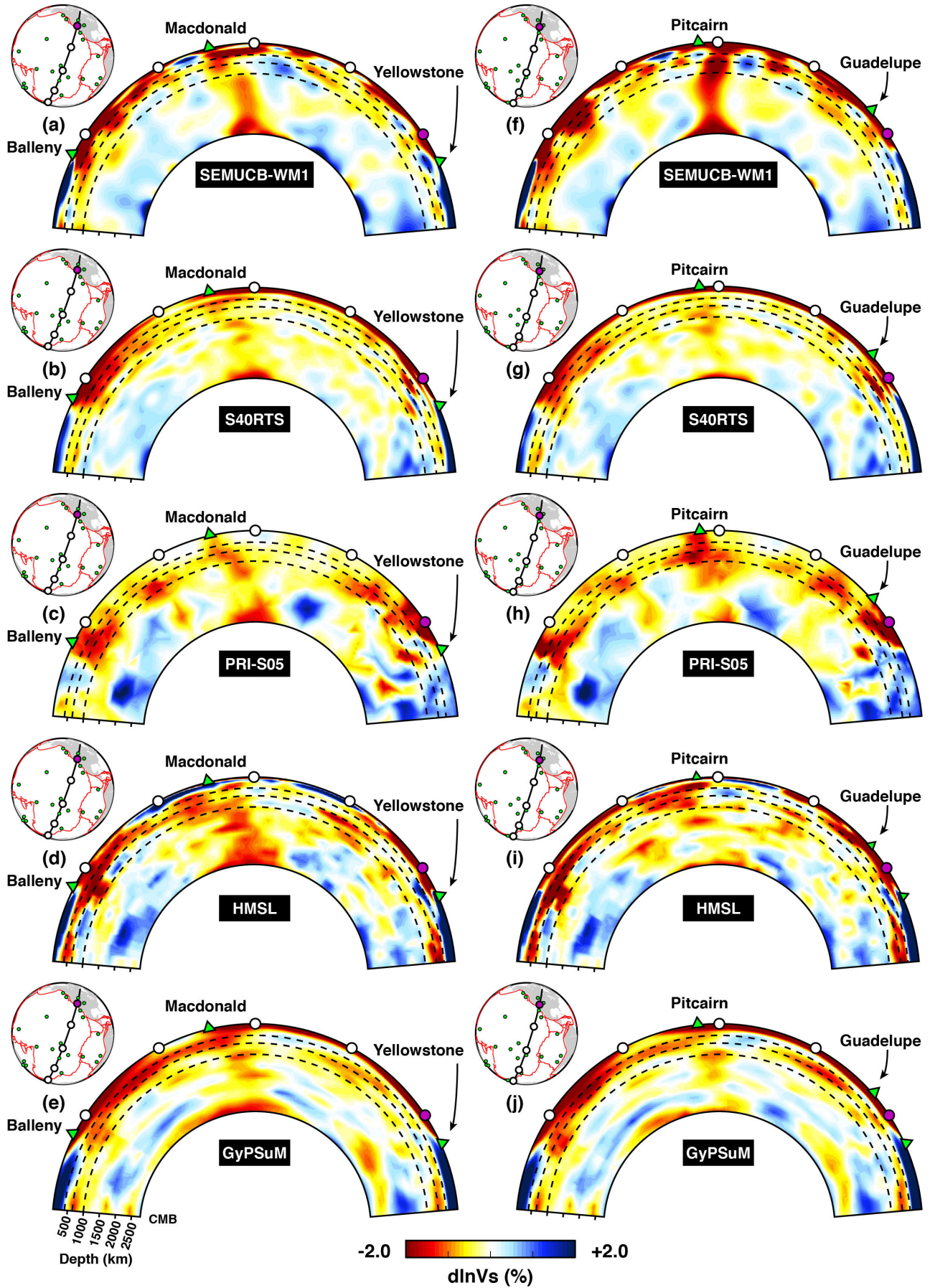
**Recovery of ‘hanging’ plume structures.** To supplement these analyses, we also explored tests using synthetic ‘hanging’ plumes—columnar anomalies extending down from the surface into the upper mantle and transition zone. These plumes have a diameter of 600 km and again a cosine-cap cross-section, as well as  $-2\%$  maximum amplitude, but are now truncated at depths of 410 km or 1,000 km (Extended Data Figs 7 and 8). This experiment is designed to further assess the effect of depth smearing, and again examines two geographic locations: Hawaii, with denser, and Iceland, with sparser, data coverage. In general, the retrieved output structures are remarkably symmetrical and exhibit the correct depth extent, with the exception of the plume truncated at 1,000-km depth beneath Hawaii,

which shows a slight eastward-trending band extending to the CMB. We note that this artefact is very weak, everywhere less than 0.1% amplitude (that is, at least 20× weaker than the −2% input amplitude). Furthermore, this artefact in no way resembles the plume we image beneath Hawaii in SEMUCB-WM1; it has a very different trend and amplitude profile. Turning now to the results beneath Iceland, we again see that retrieved amplitudes are comparatively weaker, presumably because of the sparser data coverage, but at the same time we find no anomalous band. This observation suggests that while Hawaii is expected to have denser data coverage, the data coverage beneath Hawaii might also be more anisotropically distributed. Indeed, this would be consistent with the eastward or east–southeast trending streaks seen at mid-mantle depths in some travel-time-based local tomographic studies in this region. Overall, these results give us further confidence that the depth extensions of the plumes we image in SEMUCB-WM1 cannot be attributed to smearing.

**Estimated excess temperatures and actual width of plumes.** Our resolution tests indicate that we can easily resolve a synthetic columnar velocity anomaly over a width of 1,000 km and maximum amplitude of 2% (Extended Data Fig. 4). This is indeed comparable to the maximum amplitudes of the plume conduits imaged in the mid- and lower mantle in our model. If the actual width of a plume is instead significantly smaller than 1,000 km, then the average velocity anomaly should be correspondingly larger to attain the same imaged amplitudes. For example, if the actual plume diameter is 600 km (Extended Data Fig. 5), then the actual velocity anomaly would have to be on the order of 4%–5% (as the recovered amplitudes in the 600-km-width case are on the order of  $\leq 0.5$  times those obtained for the 1,000-km-width case). Similarly, an even narrower plume, with a diameter of 400 km or less (Extended Data Fig. 6), should require a velocity contrast within the plume of more than 10% to be detected in our inversion.

Assuming the velocity anomaly is due to temperature alone, a 2% increase in  $V_s$  translates into about 200 K excess temperature ( $\Delta T$ ) in the upper mantle<sup>43,50</sup>. However, partial derivatives of shear velocity with respect to temperature greatly decrease with pressure (that is, with depth in the mantle). While they are not precisely known at lower mantle conditions, a factor-of-two reduction at mid-to-lower mantle depths is a reasonable assumption<sup>44,51</sup>, translating a 2% increase in  $V_s$  into  $\Delta T \approx 400$  K, and 10% into a most unrealistic  $\Delta T$  in excess of 2,000 K. Thus, assuming that the relative amplitude recovery in our resolution analyses is representative of reality, and that plumes are purely thermal, it is far more plausible that we are correctly resolving broader weaker plumes in the lower mantle than poorly resolving very strong narrower ones.

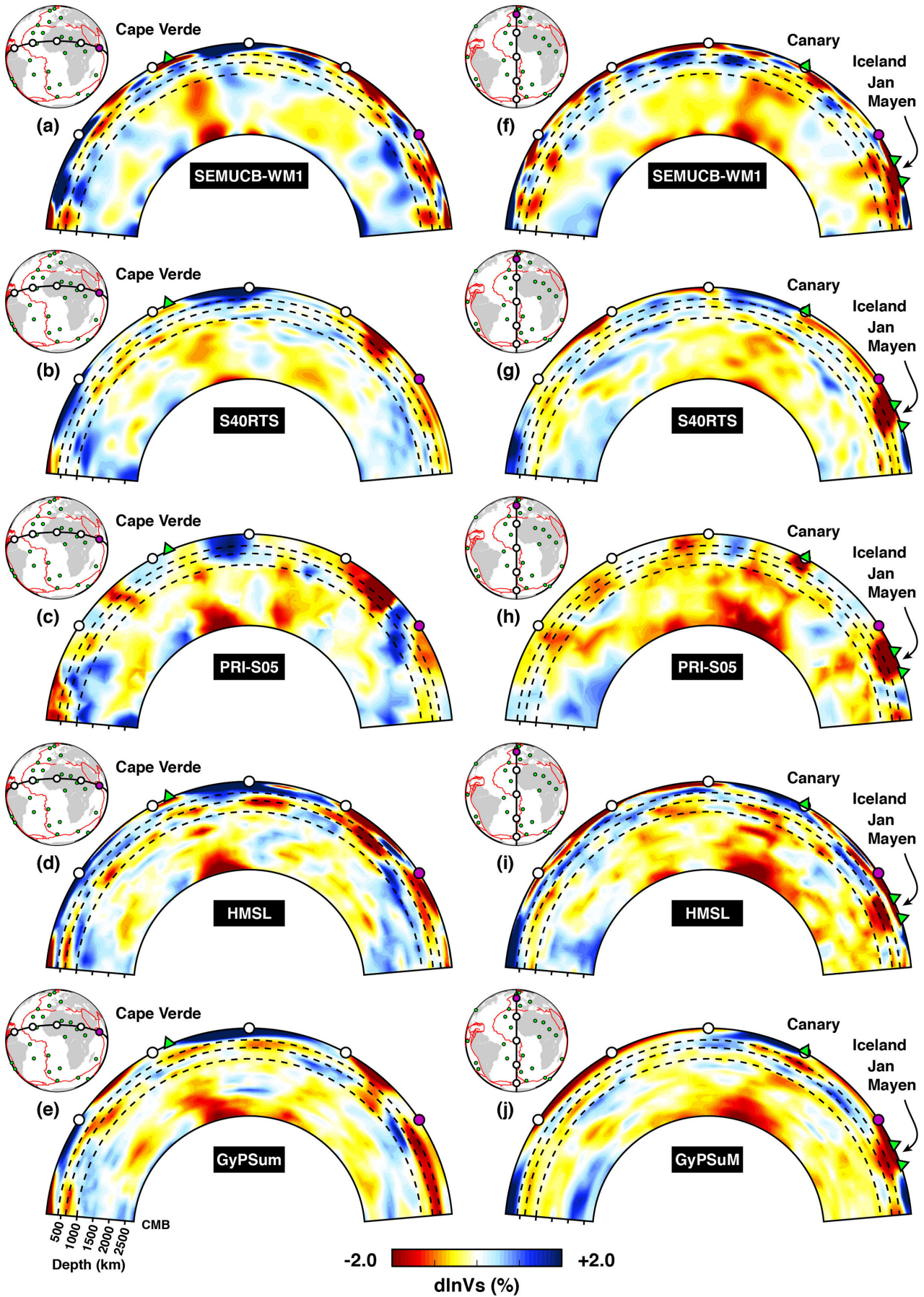
34. Lekić, V. & Romanowicz, B. Inferring upper-mantle structure by full waveform tomography with the spectral element method. *Geophys. J. Int.* **185**, 799–831 (2011).
35. Komatitsch, D. & Vilotte, J. P. The spectral element method: an efficient tool to simulate the seismic response of 2D and 3D geological structures. *Bull. Seismol. Soc. Am.* **88**, 368–393 (1998).
36. Li, X.-D. & Romanowicz, B. Comparison of global waveform inversions with and without considering cross-branch modal coupling. *Geophys. J. Int.* **121**, 695–709 (1995).
37. French, S. W., Zheng, Y., Romanowicz, B. & Yelick, K. Parallel Hessian assembly for seismic waveform inversion using global updates. In *Proc. 29th IEEE Int. 'Parallel and Distributed Processing' Symp.* (IEEE, <http://dx.doi.org/10.1109/IPDPS.2015.58>) (2015).
38. Mégnin, C. & Romanowicz, B. The three-dimensional shear velocity structure of the mantle from the inversion of body, surface and higher-mode waveforms. *Geophys. J. Int.* **143**, 709–728 (2000).
39. Durek, J. J. & Ekstrom, G. A radial model of anelasticity consistent with long-period surface-wave attenuation. *Bull. Seismol. Soc. Am.* **86**, 144–158 (1996).
40. Wang, Z. & Dahlen, F. A. Spherical-spline parametrization of three-dimensional earth models. *Geophys. Res. Lett.* **22**, 3099–3102 (1995).
41. Tarantola, A. *Inverse Problem Theory and Models for Model Parameter Estimation* (Society for Industrial and Applied Mathematics (SIAM), 2005).
42. Lévêque, J., Rivera, L. & Wittlinger, G. On the use of the checker-board test to assess the resolution of tomographic inversions. *Geophys. J. Int.* **115**, 313–318 (1993).
43. Macpherson, C. G., Hilton, D. R., Sinton, J. M., Poreda, R. J. & Craig, H. High <sup>3</sup>He/<sup>4</sup>He ratios in the Manus backarc basin: implications for mantle mixing and the origin of plumes in the western Pacific Ocean. *Geology* **26**, 1007–1010 (1998).
44. Ritsema, J., van Heijst, H. J. & Woodhouse, J. H. Complex shear wave velocity structure imaged beneath Africa and Iceland. *Science* **286**, 1925–1928 (1999).
45. Kreemer, C. Absolute plate motions constrained by shear wave splitting orientations with implications for hot spot motions and mantle flow. *J. Geophys. Res.* **114**, B10405 (2009).
46. Ritsema, J., Deuss, A., Van Heijst, H. & Woodhouse, J. S40RTS: a degree-40 shear-velocity model for the mantle from new Rayleigh wave dispersion, teleseismic traveltimes and normal-mode splitting function measurements. *Geophys. J. Int.* **184**, 1223–1236 (2011).
47. Montelli, R., Nolet, G., Dahlen, F. A. & Masters, G. A catalogue of deep mantle plumes: new results from finite-frequency tomography. *Geochem. Geophys. Geosyst.* **7**, Q11007 (2006).
48. Houser, C., Masters, G., Shearer, P. & Laske, G. Shear and compressional velocity models of the mantle from cluster analysis of long-period waveforms. *Geophys. J. Int.* **174**, 195–212 (2008).
49. Simmons, N. A., Forte, A. M., Boschi, L. & Grand, S. P. GyPSuM: a joint tomographic model of mantle density and seismic wave speeds. *J. Geophys. Res.* **115**, B12310 (2010).
50. Stixrude, L. & Lithgow-Bertelloni, C. Mineralogy and elasticity of the oceanic upper mantle: Origin of the low-velocity zone. *J. Geophys. Res.* **110**, B03204 (2005).
51. Karato, S.-I. *Deformation of Earth Materials: Introduction to the Rheology of the Solid Earth* (Cambridge Univ. Press., 2008).





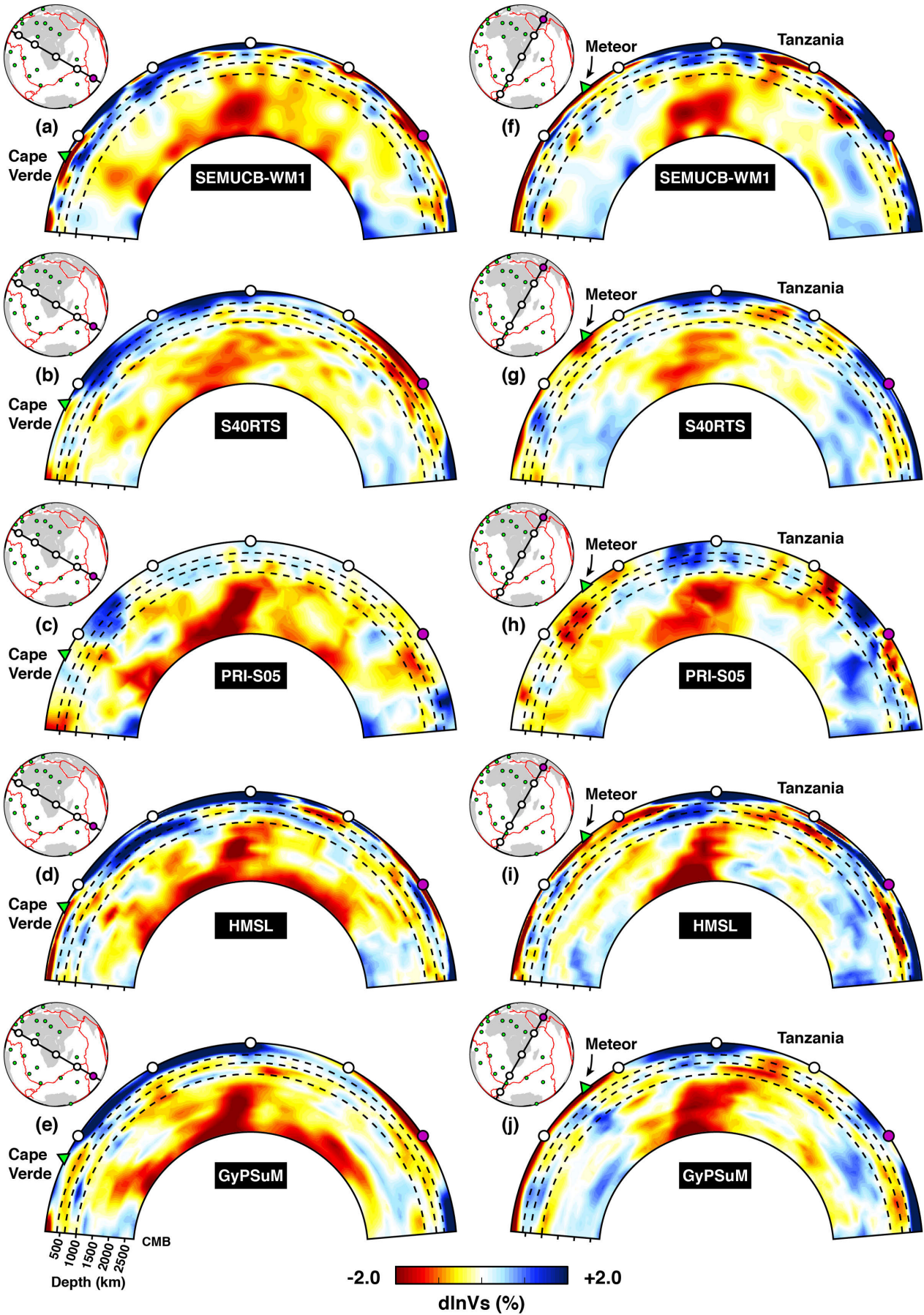
**Extended Data Figure 1 | Intermodel comparisons.** These figures correspond to the cross-sections in Fig. 1c and d, oriented normal to the direction of Pacific absolute plate motion<sup>45</sup>. As in Fig. 1, sections are indicated in the inset maps, while white and purple circles indicate position along section and orientation. Shown are relative shear-wave velocity ( $V_s$ ) anomalies in models SEMUCB-WM1 (this study), S40RTS (ref. 46), PRI-S05 (ref. 47), HMSL-S06 (ref. 48) and GyPSuM (ref. 49), each plotted with respect to its own one-dimensional reference (where the latter notion is well defined: see for example ref. 48; where defined, the one-dimensional reference is often the global

average). Panels a–e correspond to the MacDonald-hotspot-centred view of Fig. 1d; panels f–j correspond to the Pitcairn-centred view of Fig. 1c. This comparison shows that the five models are broadly compatible with each other at long wavelengths. However, in the lower mantle, the MacDonald and Pitcairn plumes are much more clearly defined as vertical conduits in SEMUCB-WM1, and stand out as the strongest and most continuous low-velocity features in the lower mantle in these cross-sections (which span almost half of Earth's circumference).



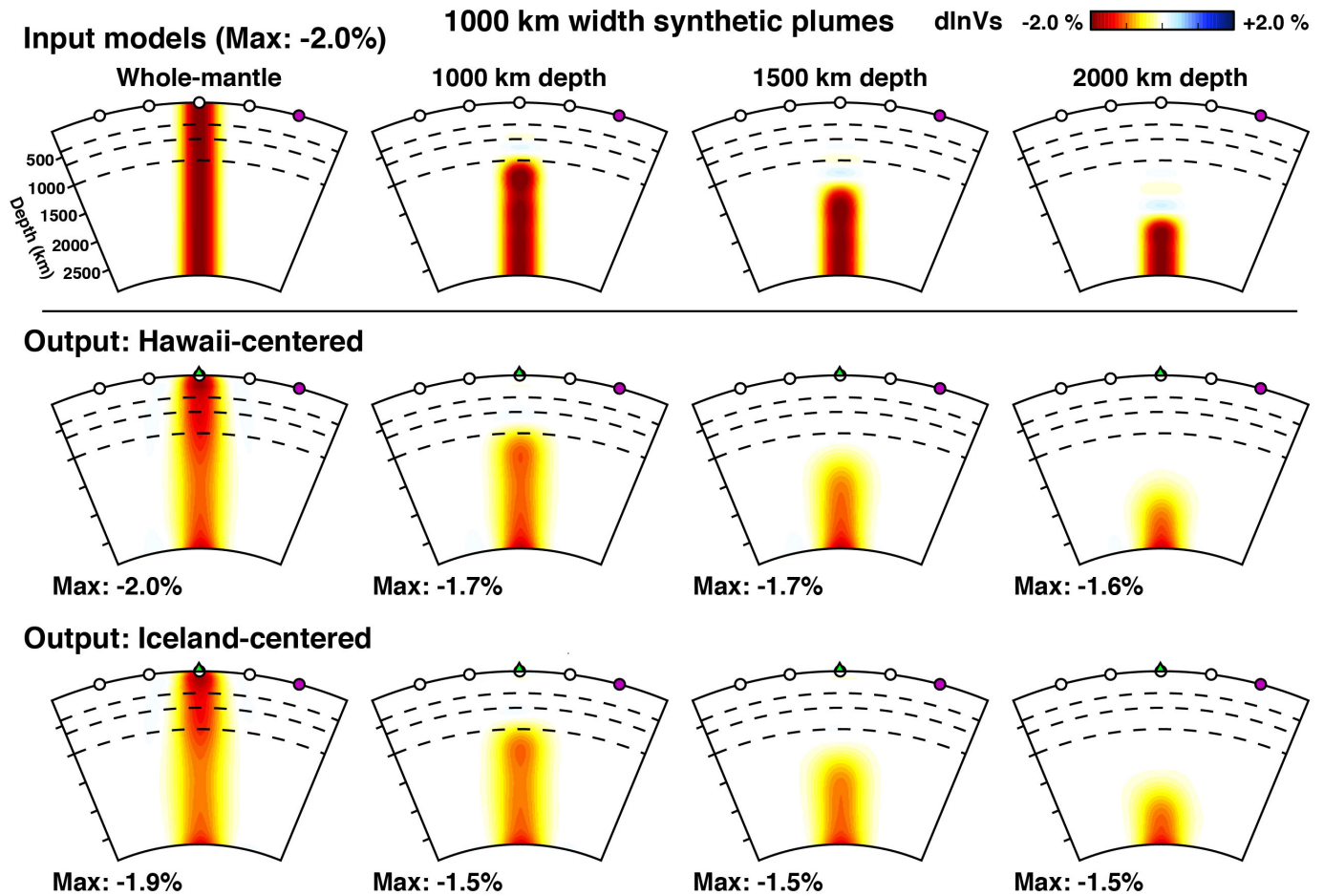
**Extended Data Figure 2 | Intermodel comparisons.** These comparisons correspond to Fig. 1e, f, presented in a similar manner to those in Extended Data Fig. 1. We again find that models SEMUCB-WM1, S40RTS, PRI-S05, HMSL-S06 and GyPSuM are broadly compatible with each other at long wavelengths. However, in the lower mantle, the plumes beneath both Cape Verde and Canary are more clearly defined as well isolated vertical conduits in

SEMUCB-WM1. Furthermore, while we do observe some degree of correspondence between the two plumes imaged in SEMUCB-WM1 and some anomalies also present in PRI-S05 or HMSL (for example, the plume root at the CMB beneath Cape Verde, or the lateral translation of the plume around 1,000 km beneath Canary), the unambiguously columnar nature of the anomalies imaged in SEMUCB-WM1 stands in stark contrast.



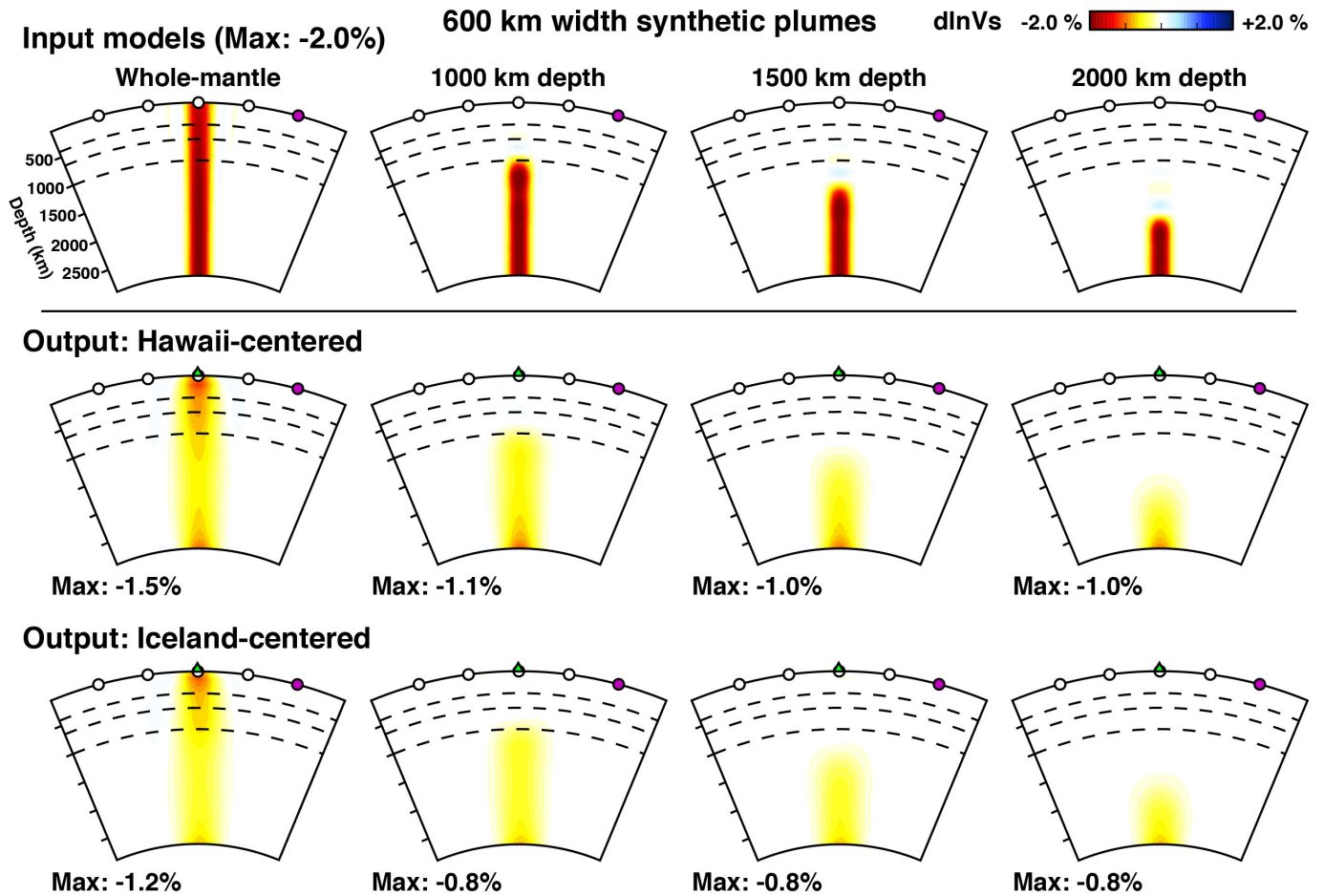
**Extended Data Figure 3 | Inter-model comparisons.** These cross-sections are similar to those in Extended Data Fig. 1, but now feature two approximately orthogonal sections through the African LLSVP: **a–e**, traversing from northwest to southeast; **f–j**, traversing from southwest to northeast. The

African LLSVP is more massive, and therefore better resolved in S40RTS, PRI-S05, HMSL-S06 and GyPSuM than are other plumes. As in Extended Data Fig. 2, we again note some degree of similarity between SEMUCB-WM1 (**a**), PRI-S05 (**c**) and HMSL-S06 (**d**) below the Cape Verde plume.



**Extended Data Figure 4 | Linear resolution analysis, examining recovery of synthetic whole- and partial-mantle plumes of width 1,000 km beneath Hawaii and Iceland.** Synthetic plume input models, shown in the upper row of panels, have a peak amplitude of  $-2\%$  and a cosine-cap lateral amplitude profile (thus, the effective width above  $1\%$  anomaly strength is only  $500\text{ km}$ ). In addition to looking at a whole-mantle plume, we also examine recovery of plumes truncated at successively greater depths ( $1,000\text{ km}$ ,  $1,500\text{ km}$  and  $2,000\text{ km}$ ) to assess vertical smearing. Artefacts seen above the truncation depth in the synthetic input models are due to slight aliasing phenomena associated with the radial b-spline basis functions used to parameterize our model. We find that all four input plumes are recovered quite well beneath both Hawaii

(centre row), with relatively denser data coverage, and Iceland (bottom row), with comparatively sparser coverage—although there is a slight difference in amplitude recovery beneath the two (maximum amplitude recovered is shown for each panel). Importantly, we see no evidence of lateral (or, in the case of the truncated plumes, radial) smearing, nor do we detect significant gaps in recovery. However, recovered amplitude does vary as a function of depth, with comparatively weaker, although still satisfactory, recovery in the less well sampled mid-mantle (of the order of half of the input anomaly strength). For a more thorough discussion of the caveats implied by linear resolution analysis in the context of our inversion, as well as additional resolution tests, see ref. 4.

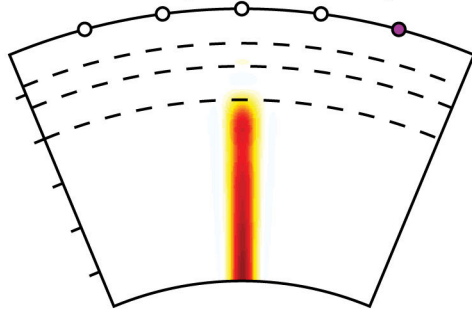


**Extended Data Figure 5 | Linear resolution analysis.** Similar to that in Extended Data Fig. 4. This analysis again features whole- and partial-mantle plumes of peak strength  $-2\%$ , but now of width 600 km (meaning the effective width above 1% anomaly strength is only 300 km). We again find that the synthetic input plumes are recovered quite well, with no evidence of lateral or radial smearing, as well as no gaps in recovery. At the same time, we find that recovered amplitude is poorer than for the larger, 1,000-km-width plumes,

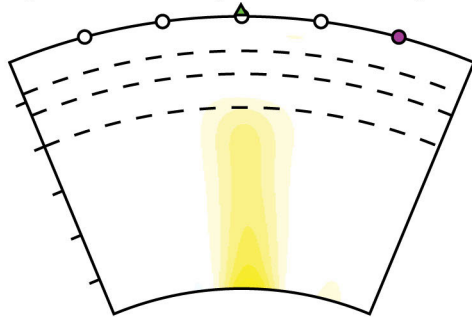
in some cases recovering amplitudes of the order of one-quarter of the input, and we note that there is again a slight disparity in amplitude recovery between Hawaii and Iceland. Furthermore, we note that tests using synthetic plumes at or below widths of 600 km push the limits of the spherical-spline lateral basis functions used in our model—particularly in the upper mantle, where the inter-spline absolute distance is larger (although the angular distance remains constant).

## 400 km width synthetic plume

Input model (Max: -2.0%)



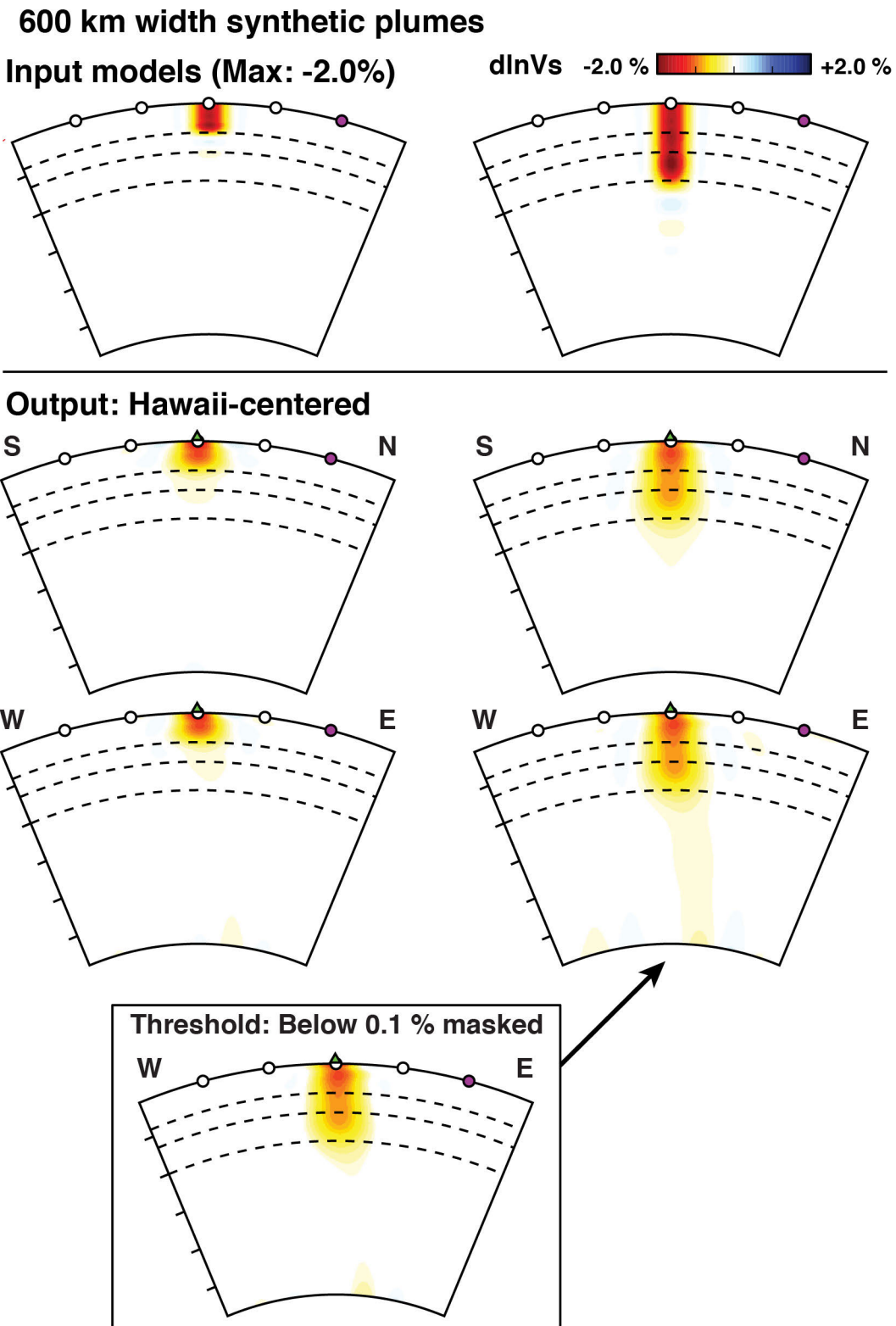
Output model (Max: -0.6%)



dlnVs -2.0%  +2.0%

**Extended Data Figure 6 | Further linear resolution analysis.** This analysis is of a 400-km-width plume-like conduit extending from the CMB to 1,000-km depth, with a similar lateral profile (a cosine cap) and maximum amplitude ( $-2\%$ ) as the test structures in Extended Data Figs 4 and 5. The inherent limits of our spherical spline basis prohibit us from representing this narrow conduit with sufficient fidelity for the purposes of this test above 1,000 km. Upper panel, conduit-like input structure; lower panel, output structure resulting from resolution test. We observe that the output structure is at least 800 km in width, but is also significantly weaker than the input, exhibiting a maximum amplitude of  $-0.6\%$  near its base, while only reaching  $-0.3$  or  $-0.4\%$  elsewhere in its core. As such, we can infer that the input-structure amplitudes would need to be increased by at least  $10\times$  in order to maintain amplitudes near  $-2.0\%$  throughout the majority of the lower mantle. This latter observation has implications for effective excess temperature (see Methods).




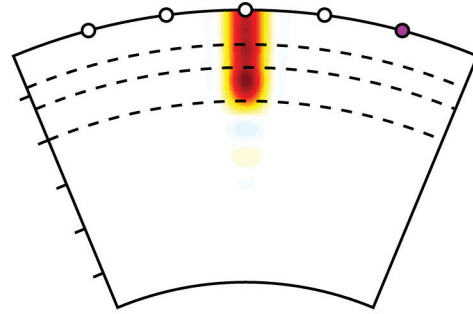
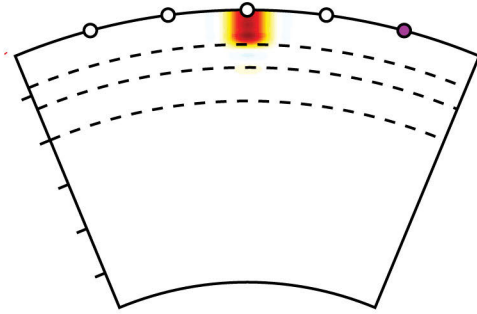


**Extended Data Figure 7 | Linear resolution analysis for synthetic ‘hanging’ plume input structures in the upper mantle and transition zone.** Like those in Extended Data Figs 4 and 5, these plumes have an overall width of 600 km and a cosine-cap lateral cross-section, as well as  $-2\%$  maximum amplitude, but are now cut at 410-km (left panels) or 1,000-km (right panels) depth. This experiment is designed to assess the effect of depth-smearing in SEMUCB-WM1. Upper panels, hanging-plume input models. Lower panels, output models when inputs are placed beneath Hawaii. We note that in general

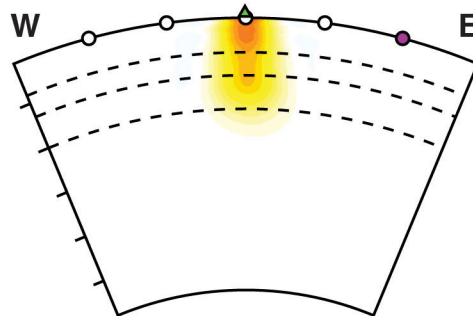
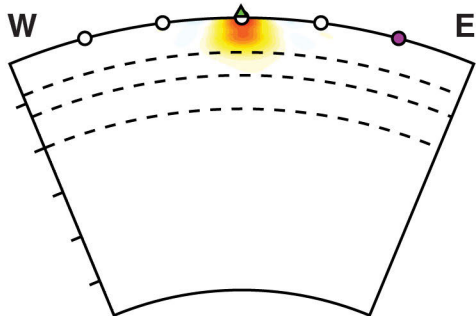
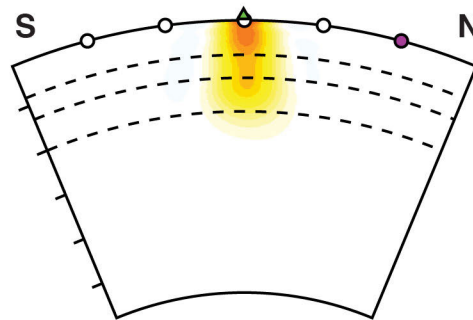
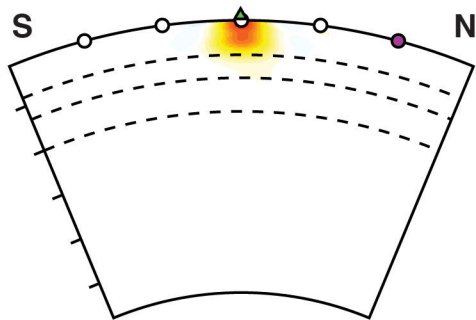
the structures retrieved are quite symmetrical and exhibit the appropriate depth extent, with the exception of the plume truncated at 1,000 km, which shows a weak eastward-trending band extending to the CMB. We note that this artefact is very weak, generally less than 0.1% amplitude, as illustrated in the bottom panel, where structure below 0.1% is masked (that is, the band is at least  $20\times$  weaker than the  $-2\%$  input structure). Furthermore, we note that this feature is not at all like the plume we image beneath Hawaii, as it possesses a very different trend and amplitude profile.

## 600 km width synthetic plumes

Input models (Max: -2.0%)

dlnVs -2.0%  +2.0%

Output: Iceland-centered



**Extended Data Figure 8 | Linear resolution analysis for synthetic ‘hanging’ plume input structures in the upper mantle and transition zone.** This figure is similar to Extended Data Fig. 7, but now examines recovery beneath Iceland. Upper panels, hanging-plume input models. Lower panels, output

models when inputs are placed beneath Iceland. The retrieved structures are again quite symmetrical and exhibit the appropriate depth extent, although amplitude recovery is slightly less impressive than that observed beneath Hawaii (consistent with the results of Extended Data Figs 4 and 5).

Extended Data Table 1 | Plumes detected in the lower mantle in model SEMUCB-WM1<sup>4</sup>, and corresponding hotspots

Index of plume (Fig. 4)	Hotspot name	Ranking by Courtillot <sup>26</sup>	Buoyancy flux <sup>26</sup>	<sup>3</sup> He/ <sup>4</sup> He <sup>26</sup>
<b>Category 1: "Primary Plume"</b>				
1	Afar	4	1	high
2	Canary	2	1	low
3	Cape Verde	2	1.6	high
4	Comores	0+	?	?
5	Hawaii	4+	8.7	high
6	Iceland	4+	1.4	high
7	Macdonald	2+	3.3	high?
8	Marqueses	2+	3.3	low
9	Pitcairn	2+	3.3	high?
10	Samoa	4	1.6	high
11	Tahiti/Society	2+	3.3	high?
<b>Category 2: "Clearly resolved"</b>				
12	Cameroon	0+	?	?
13	Caroline	3	2	high
14	Easter	4+	3	high
15	Galapagos	2+	1	high
16	Louisville	3+	0.9	?
17	Reunion	4	1.9	high
18	St Helena	1	0.5	low
19	Tristan	3	1.7	low
20	Kerguelen	2+	0.5	high
<b>Category 3: "Somewhat resolved"</b>				
21	Ascension	0+	1	?
22	Azores	1+	1.1	high?
23	Bouvet	1+	0.4	high
24	Crozet/Pr.Edw/	0+	0.5	?
25	Hoggar	1	0.9	?
26	Juan Fernandez	2+	1.6	high
27	San Felix	1+	1.6	?
<b>Not associated with any known hotspot</b>				
	Indonesia			

The numbering (column 1) and categories correspond to those in Fig. 4. Plumes are categorized as primary if the corresponding low-velocity conduit in the lower mantle has  $\delta V_s/V_s$  less than  $-1.5\%$  for most of the depth interval 1,000–2,800 km. These 11 plumes also correspond to regions of the lower mantle where the average velocity reduction over the depth range 1,000–1,800 km is significant at the  $2\sigma$  level (see, for example, Supplementary Figs 3 and 4). Clearly resolved plumes correspond to vertically continuous conduits with  $\delta V_s/V_s < -0.5\%$  in the depth range 1,000–2,800 km. Somewhat resolved plumes have vertically trending conduits with  $\delta V_s/V_s < -0.5\%$  for most of the depth range 1,000–2,800 km, albeit not as clearly continuous. The only clearly resolved plume in the lower mantle that is not near a hotspot is in Indonesia, possibly because it is rising beneath a broad slab. However, it occurs close to a location where high <sup>3</sup>He/<sup>4</sup>He ratios have been observed<sup>43</sup>. For comparison, we list the corresponding hotspot ranking (column 3)<sup>26</sup>, as well as the buoyancy flux (column 4) and <sup>3</sup>He/<sup>4</sup>He ratios (column 5)<sup>26</sup>. Question marks indicate no value given in ref. 26. Note that in this previous ranking of hotspots, these estimates of buoyancy flux and <sup>3</sup>He/<sup>4</sup>He ratios were used together with the velocity anomaly values in the transition zone (500-km depth) from an older tomographic shear-velocity model<sup>44</sup>. In contrast, our ranking is based entirely on the continuity of broad vertically oriented low-velocity structures across the major part of the lower mantle. Hotspots that do not have any clear expression in the lower mantle in model SEMUCB-WM1 are not listed, namely Yellowstone, Juan de Fuca/Cobb and Bowie (see also Fig. 4).